

Studies on Plasma Direct Energy Converters for Thermal and Fusion-Produced Ions Using Slanted Cusp Magnetic and Distributed Electric Fields

Y. Yasaka, K. Goto, A. Taniguchi, A. Tsuji, H. Takeno

Department of Electrical and Electronic Engineering, Kobe University, Kobe 657-8501, Japan

e-mail contact of main author: yasaka@eedept.kobe-u.ac.jp

Abstract. Two types of direct energy converters, cusp direct energy converter (CUSPDEC) and traveling wave (TW) DEC, used to produce electricity from thermal ions and fusion products in an advanced fueled fusion, are investigated using small-scale devices. In CUSPDEC, magnetized electrons are deflected along the field lines of the cusp magnetic field to the line cusp region and collected by an electron collector, while weakly magnetized ions can traverse the separatrix and enter into the point cusp region. Thus, ions are separated from electrons, and flow into an ion collector to produce DC power. By using a normal cusp magnetic field, the particle separation is achieved for low energy electrons, but not for electrons with much higher energies. This difficulty is overcome by applying a slanted cusp magnetic field, which has the capability of separating electrons with energies as high as 8 keV. Efficiencies of energy conversion of separated ions with large thermal spread of energy are measured to be ~55 %. An additional lateral electrode, together with the existing collector, constitutes a two-stage ion collector that provides distributed ion-decelerating fields. From the measured voltage-current characteristics, the efficiency of this collector is estimated to be improved to 65-70 %, which is consistent with the calculation. Fusion-produced fast ions enter into TWDEC and are velocity-modulated by RF fields, bunched, and then decelerated by RF traveling-wave fields on the decelerator to produce RF power. The TWDEC device has shown that the energies of ions of 3-6 keV can be decreased by 10-15 % for a one-wavelength decelerator. This would give a total efficiency of 60-70% for a full-length decelerator. A novel system is being investigated for further improvement, in which the incoming ions are deflected transversely, according to each energy, to form a fan-shaped beam and a distributed electrode array for modulation and deceleration generates traveling waves appropriate to each ion path depending on the energy.

1. Introduction

A direct energy conversion system designed for an advanced-fuel fusion reactor consists of a CUSP direct energy converter (DEC) and a Traveling Wave (TW) DEC [1,2]. The CUSPDEC device has two magnetic coils, A and B, to form the cusp magnetic field. If the density of the incident plasma is sufficiently low, electrons, which are fully magnetized, are deflected along the field line to the line cusp and collected by the electron collector. Since ions are weakly magnetized, they can traverse the separatrix and preferentially enter into the point cusp and consequently separated from electrons. They finally flow into the ion collector at a high potential to produce DC power as shown in Fig. 1. Fusion-produced fast ions (protons in D-³He reaction) enter into TWDEC and are velocity-modulated by RF fields, bunched, and then decelerated by RF traveling-wave fields on the decelerator to produce

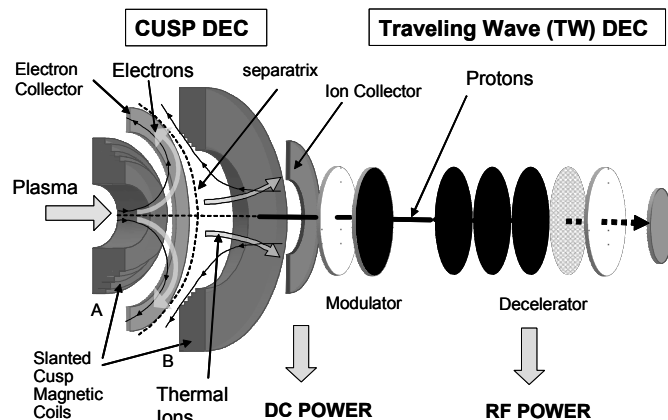


FIG. 1. Schematics of the two types of DEC's.

RF power. The RF voltage on each electrode is generated via induction of fast charged particle itself and the phase of RF is adjusted in L-C delay circuits connected to electrodes. Several experimental works have been performed to show the proof-of-principle [3,4], improved operations [5,6], and demonstration of direct energy conversion into electricity [7].

In this paper, use of the slanted cusp magnetic field in CUSPDEC, has greatly improved capability of separation of electrons with energies up to 8 keV from ions. Efficiencies of energy conversion of separated ions with large thermal spread around 1-2 keV can be increased from ~55 % to 65-70 % with an additional lateral ion collector that provides distributed ion-decelerating fields. The TWDEC device has shown that ions of 3-6 keV can be decelerated by 15-20 % for a decelerator of one-wavelength long. A novel distributed electrode system is being investigated for further improvement.

2. High Performance Operation of CUSPDEC

2.1. Basic Principle of CUSPDEC

We briefly consider the motion of charged particles in an axisymmetric magnetic field. The Störmer potential for particles with a canonical angular momentum p_θ in a system of an axisymmetric magnetic field given by the vector potential $A_\theta(r, z)$ is represented by

$$F(r, z) = \frac{m}{2} \left(\frac{p_\theta - qA_\theta(r, z)r}{mr} \right)^2, \quad (1)$$

where q is the charge, m is the mass, and $p_\theta = mr^2\dot{\theta} + qA_\theta r$, which is conserved. When the kinetic energy of the incident particle is $W = mv_0^2/2$ and no electric field is present, the particle trajectory must satisfy $F(r, z) \leq W$. Assuming that the incident particle starts at (r_0, z_0) in the cusp magnetic field where $A_\theta(r_0, z_0) = A_0$ and $v_\theta(r_0, z_0) = 0$, the particle trajectory is restricted to:

$$\left| \frac{qA_0}{mv_0} \cdot \frac{r_0}{r} \cdot \left| 1 - \frac{rA_\theta}{r_0A_0} \right| \right| \leq 1. \quad (2)$$

When the value of $|qA_0|/mv_0$ is set to be greater than 10 for the electrons, and less than 10 for the thermal ions, Eq. (2) shows that the electrons strictly follow a field line that is represented by $rA_\theta = \text{const.}$, while the ions do not. (Note that r_0/r is the order of 1.) This is the basic principle underlying the method of charge separation by the cusp magnetic field.

2.2. Experimental Setup

The CUSPDEC device consists of a guide field section, a cusp field section, electron collectors at the line cusp side, and ion collectors at the point cusp end. The main part of the device shown in Fig. 2 has two magnetic coils, A and B to form the slanted cusp field. By adjusting the current in the two coils, I_A and I_B , the field line curvature can be varied from normal to slanted cusp fields. The field lines are plotted for $I_A = 30$ A and $I_B = 20$ A as an example. The magnetic field strength at $z = -12$ cm is ~350 G, with $z = 0$ being 0.8-cm right from the

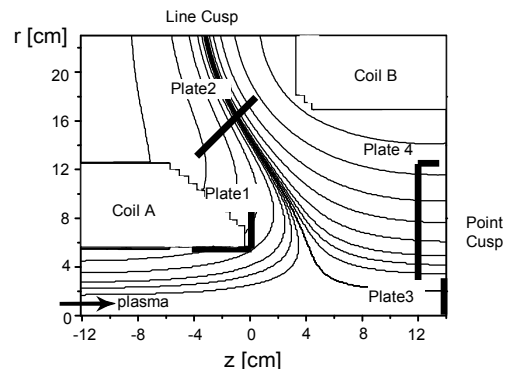


FIG. 2. The main part of CUSPDEC with the magnets (coil A and B) and collectors (Plate 1-4) and typical field lines.

right edge of the coil A. A test plasma or an end loss plasma from the GAMMA 10 tandem mirror with a diameter of about 4 cm is injected from the left side of the device into the slanted cusp field. Plane electrodes are located at the entrance line cusp (Plate 1), the line cusp exit (Plate 2), the inner point cusp (Plate 3), and the outer point cusp (Plate 4) to detect the particle flux as shown in Fig. 2. If the density of the incident plasma is sufficiently low, magnetized electrons flow along the field line to the line cusp, whereas, ions can traverse wide regions and preferentially enter into the point cusp end where the decelerating electric field is present, then finally are collected by high-potential electrodes.

The plasma in GAMMA 10 is produced and heated by ion cyclotron range of frequencies (ICRF) waves launched in the central cell, and axial confinement is established by producing an ion confining potential in the plug cells in later time by applying electron cyclotron heating (ECH). Typical line densities are $5 \times 10^{13} \text{ cm}^{-2}$ and perpendicular ion temperatures are $\sim 5 \text{ keV}$. The data from an end loss analyzer show that the maximum ion and electron energies before ECH are around 0.7 keV and 0.5 keV, respectively, and those during the ECH pulse for the potential formation are 2 keV and 3 keV or higher, respectively. The parallel ion temperature is 0.3~1 keV.

2.3. Separation of Charged Particles

When the end loss flux of GAMMA 10 is introduced to the CUSPDEC device, it is expected that electrons are deflected toward the line cusp region along the field lines. The electron current at the collector(s): (a) Plate 1 (P1, hereafter), (b) P2, and (c) P3+4 (connected in parallel) during the ECH pulse are plotted in Fig. 3 as a function of I_B / I_A . The voltages on the plates are $V_1 = 0.2 \text{ kV}$, $V_2 = 0.2 \text{ kV}$, and $V_{3+4} = 1 \text{ kV}$. For $I_B / I_A < 0.3$, most of the field lines at the entrance connect to P3+4, and the electron current appears on these plates with no current on P1 and P2. As the value of I_B / I_A becomes larger up to ~ 1.0 , electrons flow into P2 along the field lines and the current on P3+4 decreases due to the separatrix formed at $z = 0 \sim 5 \text{ cm}$. Further increase of I_B / I_A from ~ 1.0 to 1.3

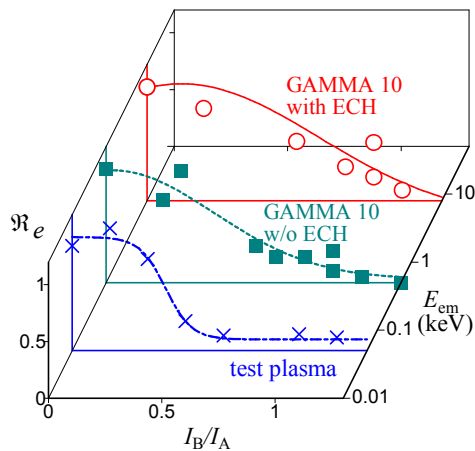


Fig. 4. Fraction of non-separated electrons \mathcal{R}_e as functions of I_B / I_A .

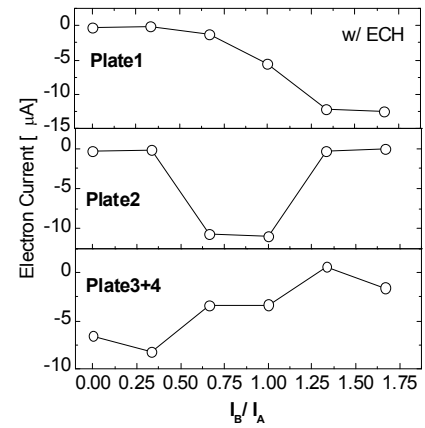


Fig. 3. The electron currents at the collector(s), from top to bottom, Plate 1, Plate 2, and Plate3+4.

results in increase of the field line curvature and the field lines are bent to touch P1. As a consequence, the electron current on P2 decreases, while it increases on P1. P3+4 still collects electrons until I_B / I_A exceeds 1.25 because of the high positive potential applied on it. By setting $I_B / I_A = 1.3$, almost complete elimination of electrons at the point cusp region has been achieved.

Figure 4 shows the fraction of electrons that crosses the separatrix to the point cusp, \mathcal{R}_e , as functions of the degree of the slant, I_B / I_A , and the highest energy of electrons E_{em} in incident plasma beams from the test plasma source and the end loss of GAMMA 10. It is found that, for the normal cusp of $I_B / I_A = 0.4 - 0.6$,

\mathfrak{R}_e can be decreased to less than 0.25 for E_{em} of 0.05 keV or smaller, while \mathfrak{R}_e is 0.4–0.9 for E_{em} of 0.5–8 keV. The reason for this is found that the high energy electrons do not follow the field lines due to a high potential applied to the ion collector for ion deceleration. This difficulty is overcome by applying the slanted cusp magnetic field ($I_B / I_A = 0.8$ and higher). The values of \mathfrak{R}_e can be reduced to less than 0.1 even for E_{em} of 8 keV when the slanted cusp field of $I_B / I_A > 1.2$ is used.

2.4. Direct Energy Conversion from Ions

After the ions and electrons are separated by the slanted cusp magnetic field, it is necessary to decelerate and collect ions in order to recover their kinetic energy and generate electricity. In Fig. 5, the open circles represent the current to the P3+4, the ion collector, when the voltage on the collector, V , is changed for $I_A / I_B = 30 / 40$ A with ECH on. The solid line is drawn by assuming that the energy distribution function $f(E)$ of incoming ions is a shifted Maxwellian with the temperature T and the energy shift E_s , and

by calculating $I \propto e \int_{eV}^{\infty} E^{-1/2} f(E) dE$. The values

of T and E_s are determined so that the calculated I fits to an experimental V - I curve. The average energy of the ions is given by

$E_0 = \int_0^{\infty} E f(E) dE$. For the case of Fig. 5, the

best fit to the experimental points is obtained when we choose $T = 0.73$ keV and $E_s = 0.5$ keV. The value of E_0 is 1.25 keV and the degree of energy spread of $f(E)$ is $\Delta E / E_0 = 0.82$, where ΔE is the full width at the half maximum of $f(E)$. When V is set to an appropriate value, the majority of ions is decelerated to almost zero velocity and flows into the ion collector at a high positive potential. A load resistor connected to the ion collector would obtain electric power, which is directly converted from kinetic energy of incoming ions. We plot the output power P_{3+4} , the product of I and V , by the

dotted line in Fig. 5, which has a maximum at a certain voltage V_{opt} that is optimum for power conversion. The energy conversion efficiency η_s related to the shape of $f(E)$ is defined by

$$\eta_s = P_{3+4}(V = V_{opt}) / (I_0 \cdot E_0), \quad (3)$$

where $I_0 = I(V = 0)$. In the case of Fig. 5, the power output of ~ 1.3 mW with $\eta_s = 0.57$ is obtained for $V_{opt} = 1.0$ kV.

2.5. Two-Stage Deceleration by Using Distributed Electric Fields

In Sec. 2.4, we see that the efficiency of energy conversion is about 0.55, which is higher than for usual thermal conversions, but is not high enough as a high performance DEC. This is due to a large spread of the energy distribution function of incoming thermal ions. Closed symbols plotted in Fig. 6 represent the values of η_s as a function of $\Delta E / E_0$ for the test plasma and the GAMMA10 plasma with and without ECH. It is clearly seen that η_s decreases as $\Delta E / E_0$ increases. The dotted line in Fig. 6 is the calculated value of η_s for the parabolic

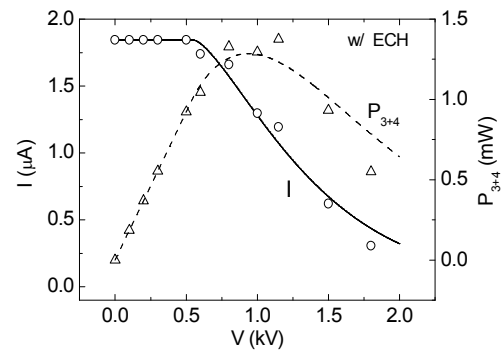


Fig. 5. Measured voltage-current characteristic of the ion collector (circles) and output power (triangles) during ECH and calculated V - I characteristics (solid line) and output power (dotted line) assuming the shifted Maxwellian energy distribution of ions.

shape of $f(E)$ with the assumption that the decrease in η_s due to the electron current to the ion collectors is 5 % regardless of the value of $\Delta E / E_0$. In these experiments, since the energy of the primary ions is low, the charge exchange with and the ionization of the residual gas are negligible. Therefore, the loss of I_0 would be produced by the secondary electrons from the Plates (1 or 2) or the wall. The loss of I_0 is estimated from the electron current at large V in the V - I curve of the ion collector to be 5–10 % reducing η_s approximately by 5 %.

In order to improve the conversion efficiency for large $\Delta E / E_0$, we employ a two-stage deceleration configuration by using existing electrodes. Calculation of particle trajectories shows that the ions with initial energies greater than eV_{3+4} flow into P3+4, while the lower-energy ions are reflected from P3+4 and their trajectories mostly intersect with P1 for some range of the slant. The electrons are deflected along the field line toward P2 except for small fraction of near-axis incidence. The degree of the slant of the magnetic field lines is sufficient to separate electrons from ions. Thus, we use P1 as a second stage ion collector to collect ions reflected from the primary ion collector P3+4. P2 could be used as the electron collector, but is left floating in this experiment. The measured V - I characteristics of the primary ion collector P3+4 and the secondary collector P1 are plotted in Fig. 7 when changing the voltage V_{3+4} on P3+4 for a fixed $V_1 = 0.2$ kV. As V_{3+4} is increased, the current on P3+4 decreases due to the reflection of low-energy ions from the primary collector and the current on P1 increases accordingly. If we use only P3+4 as the ion collector, the efficiency of energy conversion of ions given by Eq. (3) is found to be 0.56 with $\Delta E / E_0 = 1.19$. This value of $\eta_{S \text{ 1-stage}}$ is similar to those of $\Delta E / E_0 \sim 1$ shown in Fig. 6. On the other hand, the use of the secondary ion collector in addition to the primary one yields, using $P_{3+4}^{\text{opt}} + P_1^{\text{opt}}$ instead of P_{3+4}^{opt} in Eq. (3), $\eta_{S \text{ 2-stage}} \sim 0.64$, resulting in the improvement in efficiency of 8 %.

We estimate the efficiency of energy conversion in the two-stage deceleration scheme. For a given energy distribution function of incident ions and a voltage on V_{3+4} , the energy distribution of reflected ions flowing into P1 can be determined. In this case, some ions do

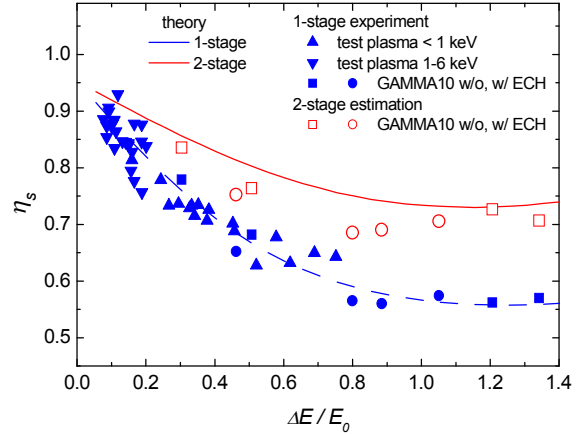


Fig. 6. The measured value of η_s versus $\Delta E / E_0$ of the ion flux for the low energy plasma source (closed triangles) and for GAMMA 10 (closed circles and rectangles). Open symbols show the estimated η_s for the two-stage deceleration. The dotted and solid curves indicate calculated efficiencies for the one- and the two-stage cases.

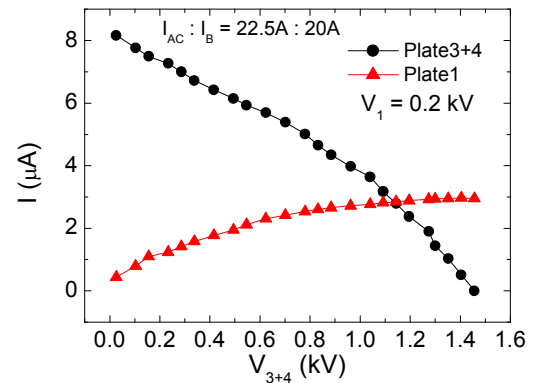


Fig. 7. Measured voltage-current characteristic of the primary ion collector P3+4 (circles) and the secondary collector P1 (triangles) for a fixed $V_1 = 0.2$ kV. The value of $\Delta E / E_0$ is 1.19.

not reach P1 and some ions lose their effective energy by a change in v_θ . Typically, 75 % of reflected ions flow into P1 with others to the wall, and the average energy decrease is 5 %. The output power on P1 at V_1 is calculated from V - I characteristics on P3+4 in Fig. 7. The calculation is repeated by changing V_1 and V_{3+4} to obtain Fig. 8 that shows contour lines of $\eta_{2\text{-stage}}$ on V_1 - V_{3+4} plane for ions with $\Delta E/E_0 = 1.19$. The maximum value is 71.4 % when $V_{3+4} = 1.38$ kV and $V_1 = 0.62$ kV. We note that the efficiency of the two-stage conversion for separated ions can be 70 % or higher in comparison to the one-stage case where the efficiency is ~ 55 % for the values of $\Delta E/E_0$ around 1. Experimental data points are given in Fig. 8 for the two-stage (circle) and one-stage conversion (rectangle). The calculated efficiency for this setting is about 62-63 %, which is close to the experimental value. The open symbols in Fig. 6 indicate η_S estimated from the measured V - I characteristics of P3+4 corresponding to some experimental points. Improvements more than 10 % are estimated, which are consistent with the differences of the calculated values for the 2- (solid curve) and the 1- (dotted curve) stage cases. The second collector is laterally displaced from the primary one and would not affect the motion of ions flowing into the primary collector. For higher incoming flux, collective phenomena may appear to drive instabilities or orbit losses, which are under investigation.

3. Improved Configuration for TWDEC

3.1. Basic Principle of TWDEC

The TWDEC device shown in Fig. 1 consists of the modulator and the decelerator, where, respectively, the beam of protons is velocity-modulated by the self-induced RF fields to form a bunch downstream, and is decelerated by the self-induced RF traveling wave. Here, we assume that the RF fields are externally excited by applying phased RF voltage on grid arrays for simplicity. Figure 9 shows the calculated phase space diagrams for protons with the initial energy of $E_B = m_p u_B^2/2 = 14.7$ MeV in TWDEC with the 1-wavelength (λ_0) long modulator (M) of $eV_{\text{mod}}/E_B = 0.03$ and the decelerator (D) of $eV_{\text{dec}}/E_B = 0.082$ for (a) $\Delta E/E_B = 0.001$ and (b) $\Delta E/E_B = 0.13$. The inset shows $f(E)$ at the exit of D. The value of λ_0 is 6.28 m and the RF is at $f = u_B/\lambda_0 = 8.46$ MHz. The decelerator has 4 electrical wavelength (4 stage of λ), where the real length is $8\lambda_0/3$ since λ becomes shorter along

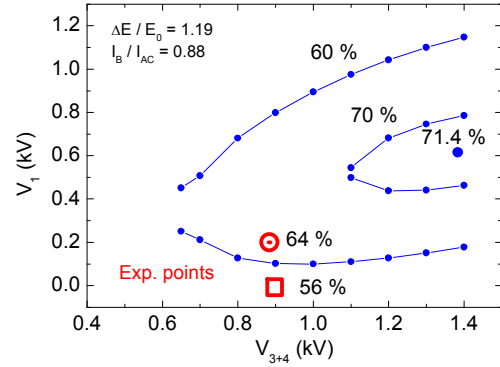


Fig. 8. Contour lines of the efficiency of the two-stage energy conversion on V_1 - V_{3+4} plane. Experimental data are given for the two-stage (circle) and one-stage conversion (rectangle).

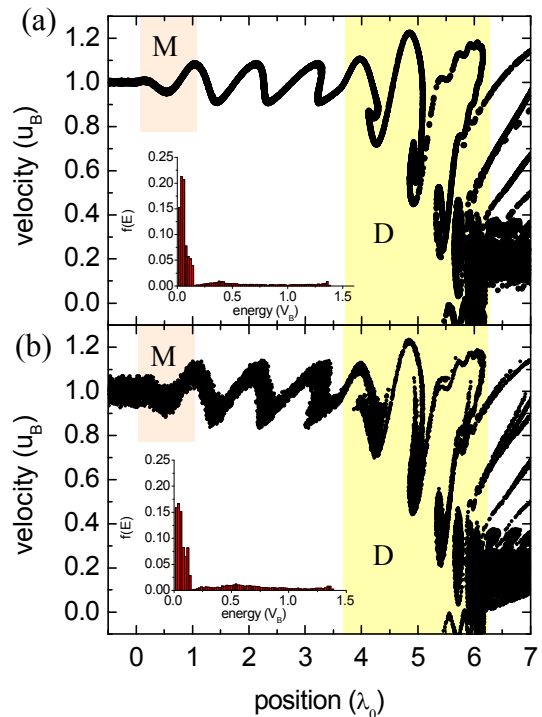


Fig. 9. Calculated phase space diagrams for protons with the initial energy of $E_B = m_p u_B^2/2 = 14.7$ MeV for (a) $\Delta E/E_B = 10^{-3}$ and (b) $\Delta E/E_B = 0.13$. The inset shows $f(E)$ at the exit of D.

with slowing down of the particles. It is seen that most of the protons are decelerated in latter stage in the decelerator down to almost zero. The efficiency of energy conversion may be calculated from the rate of reduction in average kinetic energy $\langle E \rangle$ given by $\eta_{\text{TW}} = (\langle E \rangle_0 - \langle E \rangle) / \langle E \rangle_0$, where $\langle E \rangle_0 = E_B$ is the average energy of the incident beam. By evaluating $\langle E \rangle$ from $f(E)$ at the decelerator exit shown in the inset of Fig. 9, we find that $\eta_{\text{TW}} = 0.815$ for (a) and 0.731 for (b). The degradation in η_{TW} due to the thermal spread in velocity of the incident beam is $\sim 8\%$.

3.2. Comparison with Small-Scale Experiment

The solid lines in Fig. 10 indicate the value of η_{TW} for the decelerator length of one λ , $\eta_{\text{TW}1}$, as a function of the total decelerator length in the unit of λ for various V_{dec}/E_B with the other parameters the same as in Fig. 9 (b). The integral of each curve gives the total efficiency η_{TW} given above. The value of $\eta_{\text{TW}1}$ is 10-20 % for the first 1 or 2λ region in the decelerator. Open circles in Fig. 10 are the results from small-scale experiments with $E_B = 3-6$ keV, $\Delta E/E_B \sim 0.1$, $eV_{\text{mod}}/E_B = 0.1-0.15$, and $eV_{\text{dec}}/E_B = 0.05-0.1$. Note that use of normalization: length by λ_0 , time by f^{-1} , and energy by V_B reduces the systems equivalent regardless of absolute values of V_B . Considering that the values of eV_{mod}/E_B and eV_{dec}/E_B for the experiment are scattered, we see that the experimental result is consistent with that of the numerical calculation.

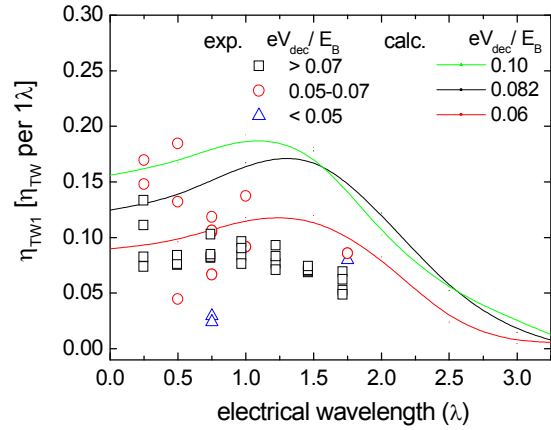


Fig.10. Efficiency of energy conversion per 1λ versus the decelerator length in the unit of λ for various eV_{dec}/E_B . Symbols are data points from the small-scale experiment.

3.3. A Novel Type of TWDEC Using Distributed Electric Fields for Higher Performance

In TWDEC, phase relation between the bunched ion beams and the traveling waves is very important for high conversion efficiencies. Even for 10-% energy spread, which is typical for protons in D-³He reaction due to thermal effects, it is calculated that the phase relation cannot be maintained along the ion path resulting in 8-15 % degradation in efficiencies, as partly seen in Fig. 9. This is due to the fact that particles with off-centred velocity are not in-phase with the decelerating RF field. We use a configuration shown in Fig. 11 where the beam particles follow fan-shaped trajectories according

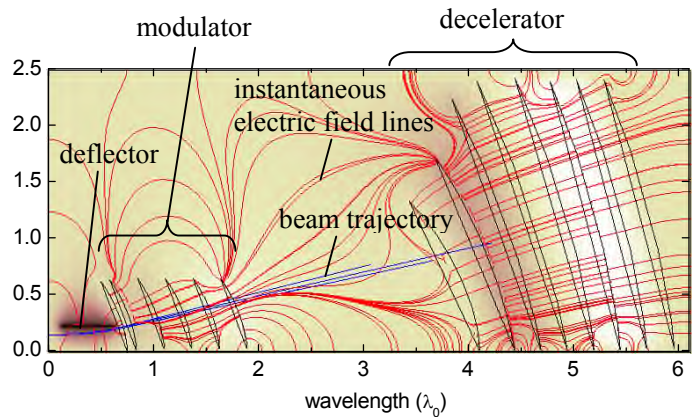


Fig.11. Schematic diagram of a novel TWDEC using distributed electric field to achieve higher efficiency.

to each energy and a distributed electrode array of modulator and decelerator generates RF traveling waves appropriate to each ion trajectory depending on the energy. A localized transverse magnetic field will be used as a deflector. This enables all the particles with different velocities to maintain appropriate phase relation with RF. We use a simple 2-D code to calculate the potential distribution for a given electrode array and the trajectory of test particles injected with a velocity determined by a given energy distribution function. Figure 12 depicts the positions of all protons of the initial energy of 14.7 MeV with colors corresponding to the value of kinetic energy of protons. Slower protons are deflected downwards at the very end of the decelerator being separated from protons that are not well decelerated. In Fig. 12, a total efficiency of deceleration of 68 % is obtained. We will optimize the configuration to achieve efficiencies close to the value for the case of monochromatic $f(E)$.

4. Summary

In summary, we have shown that the two types of the DEC devices work as expected for keV-class charged particles. The lateral two-stage ion collector combined with the slanted cusp is expected to improve the efficiency from $\sim 55\%$ to $65\text{--}70\%$ in CUSPDEC. In TWDEC, the deceleration efficiencies of $10\text{--}15\%$ for one-wavelength has been obtained in the small-scale experiment, and are essentially scalable to the calculation results for 14.7-MeV protons that give a total efficiency of $\sim 70\%$. A novel TWDEC device is proposed in order to eliminate the effect of thermal spread of the beam that degrades the efficiency. Preliminary calculation has revealed basic operation of the device.

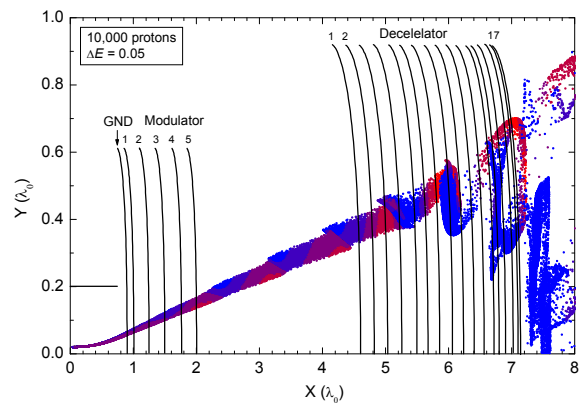


Fig.12. Accumulated plot of particle positions in the fan-shaped TWDEC. Each color corresponds to the value of kinetic energy.

Acknowledgments

We thank Drs. Y. Nakashima and T. Imai for arrangements of the GAMMA 10 experiments. This work was partly carried out under the bilateral collaboration research of Kobe University, Plasma Research Center, Univ. Tsukuba, and National Institute for Fusion Science.

References

- [1] Momota, H., et al., *Fusion Technol.* **21** (1992) 2307.
- [2] Momota, H., et al., *Proc. 7th Int'l. Conf. on Emerging Nuclear Energy Systems (Makuhari, Japan, September 1993)* (Singapore: World Scientific, 1993) p 16.
- [3] Yasaka, Y., Inoue, K., Tomita, Y. Momota, H., *Trans. Fusion Technol.* **43** (2003) 312.
- [4] Noda, K., Yasaka, Y., *Fusion Technol.* **33** (1998) 273.
- [5] Yasaka, Y., et al., *Fusion Sci. Technol.* **47** (2005) 455.
- [6] Takeno, H., et al., *Jpn. J. Appl. Phys.* **39** (2000) 5287.
- [7] Yasaka, Y., et al., *Nucl. Fusion* **48** (2008) 035015.